Separation and Purification Technology 366 (2025) 132829

Contents lists available at ScienceDirect

Separation and Purification Technology

journal homepage: www.elsevier.com/locate/seppur

Low pressure thin film membranes with cellulose nanocrystals derived from Cannabis sativa for enhanced dye and salt removal

Khona Maziya [a], Izak Kotze [a], Oranso T. Mahlangu [b], Heidi Lynn Richards [a,*]

[a] Molecular Sciences Institute, School of Chemistry, University of the Witwatersrand, Private Bag X3, Johannesburg 2050, South Africa
[b] University of South Africa, Nanotechnology and Water Sustainability Research Unit, College of Engineering, Science and Technology, Florida Science Campus, Roodepoort, South Africa

ARTICLE INFO

Editor: M. Freire

Keywords:
Cellulose nanocrystals
Glutamic acid
Thin film nanocomposite membranes
Dyes

ABSTRACT

Cellulose nanocrystals (CNCs) are gaining popularity as nanomaterials in membrane-based separation processes due to their environmental friendliness and sustainability. Thin film nanocomposite (TFN) membranes containing glutamic acid modified CNCs dispersed within a polyamide (PA) film were produced in this study using an interfacial polymerization (IP) reaction over a polysulfone (PSF) substrate for low-pressure nanofiltration (NF). To characterize the membranes, FTIR, SEM, AFM, and contact angle analysis were utilized. The resulting CNC-GLU TFN membranes (0.10 wt%) were more hydrophilic and smoother than the comparable thin film composite (TFC) membrane. The CNC-GLU TFN membrane outperformed pristine TFC membranes with a pure water flux of 15.45 ± 1.03 L/m^{2}h (400 kPa), high dye rejection (99.83 % for methylene blue, 90.63 % for methyl orange) and salt removal ($MgSO_4$ = 86 %; NaCl = 38 %). This was attributed to the increased hydrophilic active layer, Donnan exclusion, and steric hindrance. Furthermore, the TFN membrane effectively removed MB and MO dyes from wastewater and demonstrated good operational stability after six cycles. These findings revealed the enormous potential of these membranes in wastewater treatment, separation, and purification in a wide range of industrial applications.

1. Introduction

Dyes used in the paper and textile sectors are one of the principal water pollutants, with over 10,000 tons discharged globally each year [1–3]. Dye wastewater contains elevated biological oxygen demand (BOD), chemical oxygen demand (COD), heightened color and contains organic compounds which are carcinogenic and mutagenic [4,5]. It is vital to remove dyes from textile and dyeing industries wastewater prior to being released to the environment. Dyes, even at low concentrations are toxic, and highly visible thus degrading the visual appeal of water-bodies and reducing the photosynthetic activities of aquatic flora [6,7].

Membrane separation technologies outshine conventional removal methods (adsorption, coagulation, flocculation, ozonation, etc.) due to their low operational costs, simple operation, smaller footprint and excellent selectivity [8–10]. However, conventional polymeric membranes are disposed to fouling thus reducing its lifespan [11,12]. Furthermore, the balance that exists amidst permeability and selectivity restricts the applicability of polymeric membranes [13,14]. To address these limitations, thin film nanocomposite (TFN) membranes with selective polyamide (PA) layer atop a support layer was developed. TFN membranes can be designed and controlled to regulate its separating abilities [15]. Considering only a small number of nanoparticles are required, including them into the selective PA layer lowers costs [15]. TFN membranes prepared via interfacial polymerization (IP) method on a porous support have demonstrated a high level of dye removal in water [15–18].

The integration of advanced nanomaterials into TFN membrane has been seen to significantly enhance water permeability and dye rejection performance. Ghaemi et al. (2018) investigated the effects of introducing nano-porous SAPO-34 (silicoaluminophosphate nano-porous zeolite) nanoparticles into the active layer of TFN membranes on membrane permeability and performance [19]. Upon the introduction and growth of nanoparticles in the active layer, the pure water flux increased from 10.9–35.2 kg/m^{2}h. The membrane's performance was evaluated in the removal of 50 mg/L of dyes (acid blue 193, methyl violet 6B, and reactive blue 4) in water, and the modified membranes efficiently removed 100 % of all dyes [19]. Zhao et al. (2019) evaluated the impact of graphene oxide (GO) quantum dots on membrane

* Corresponding author.
E-mail address: heidi.richards@wits.ac.za (H.L. Richards).

https://doi.org/10.1016/j.seppur.2025.132829
Received 27 February 2025; Received in revised form 28 March 2025; Accepted 1 April 2025
Available online 2 April 2025

performance [20]. Surface coating was used to incorporate GO quantum dots into the TFN PA layer, and membrane rejection against methyl orange (MO) and methylene blue (MB) was investigated. Electrostatic repulsion boosted MO rejection from 89.2 to 97 % after modifying the PA layer with GO quantum dots [20]. However, there was a drop in MB rejection (75.4–71 %), which was caused by positively charged MB adsorption onto the membrane, which reduced water flux and rejection [20].

Various materials have been incorporated during polyamide layer fabrication process to enhance water flux, selectivity and mechanical strength [21]. These include graphene oxide (GO), halloysite nanotubes (HNTs), carbon nanotubes, metallic organic frameworks (MOFs), titanium dioxide (TiO_2), etc. [18,20,22–28]. Nevertheless, some materials incorporated into TFN membranes have been documented to be toxic to humans and the environment, thus limiting their usage in water treatment [29]. Cellulose nanocrystals (CNCs) from the cellulose nanomaterial family address these concerns. CNCs are made from sustainable and renewable resources, resulting in reduced health, environmental, and safety impact [30,31]. Acid hydrolysis is one of the methods of producing rod-shaped CNCs from plant sources such as hemp, wood, wheat, etc. CNCs have several impressive attributes such as large negative surface charge density, high aspect ratio, excellent mechanical properties and hydrophilicity due to the abundance of hydroxyl groups [32–34]. These features make CNCs appealing candidates for increasing membrane performance. Furthermore, because of cellulose biomass abundance in nature and the CNC synthesis process being straightforward, CNC production is extremely cost effective, making them an attractive choice [32]. Several researchers have reported the use of CNCs in TFN membranes to enhance performance. Bai et al. (2019) investigated membrane performance following the incorporation of CNCs (0.005–0.200 wt%) in polyamide layer generated via interfacial polymerization in TFC membranes [29]. The developed membranes demonstrated excellent divalent salt rejection of 98 % and 97.5 % for $MgSO_4$ and Na_2SO_4. The membranes also demonstrated superior dye removal (Rose Bengal, Crystal violet, Congo red, Methyl orange and Methylene blue), with the 0.150 wt% CNC membrane surpassing the others with 99.0 % removal for all dyes [29].

Despite being shown to increase membrane performance, the aggregation of CNCs (stemming from hydrogen bonding interactions at the surface) remains a barrier to their widespread implementation in water treatment [33,35]. CNCs modification is crucial to address this issue. Abedi et al. (2023) demonstrated that incorporating modified CNCs into TFN membranes significantly enhanced water permeability [36]. L-cysteine-functionalized CNCs (CysCNCs) and acetylated CNCs (ACNCs) were synthesized and integrated into the membranes [36]. Among the tested membranes, CysCNC-TFN0.2 (0.2 wt% CysCNCs) achieved the highest water permeability at 16 L/m^2h.bar, followed by ACNC-TFN0.1 (14.5 L/m^2h.bar), CNC-TFN0.1 (11.5L/m^2h.bar), and unmodified TFC membranes (6 L/m^2h.bar) [36].

Polymerization is one strategy that can be utilized to modify CNCs. This technique entails exploiting the oxygenated groups located on the CNCs surface to enhance interlayer distance. Surface-initiated atom transfer radical polymerization (SI-ATRP) serves as a flexible polymerization process which produces excellent grafting density and control over the brush design and thickness. This process requires immobilizing an initiator on the substrates surface followed by the growth phase characterized by the recurrent addition of monomers on the growing chain (polymerization) [37,38]. This functionalization produces multifunctional materials with end group functionalities [39]. Modifying the surface characteristics of CNCs serves dual purposes: it elevates membrane functionality by enhancing resistance to fouling and improving separation efficiency, while simultaneously enhancing compatibility with the polymer matrix through better dispersion and reduced particle clustering.

In this work, CNCs were modified with glutamic acid brushes through SI-ATRP to develop novel TFN membranes that display improved water permeability and dye/salt rejection capabilities. A range of characterization techniques including SEM, FTIR, NMR, XRD, TGA and AFM were employed to assess the physicochemical attributes of both the CNCs and the resulting TFN membranes, thereby elucidating the influence of the modified CNCs on membrane performance. Furthermore, permeation flux and dye removal tests were used to gauge the filtration and fouling resistance of the membranes. This research represents a groundbreaking approach in applying glutamic acid-modified CNCs to boost the efficacy of TFN membranes for dye and salt removal, proposing novel and effective methodologies for producing high-performance nanofiltration membranes. Ultimately, the efficacy of the TFN membranes was evaluated in real-world applications, specifically targeting water samples contaminated with dyes.

2. Materials and methods

2.1. Materials

Sodium hydroxide (NaOH), N,N,N,N,N‴- pentamethyldiethylenetriamine (PMDETA, 99 %), glacial acetic acid (CH_3COOH), sodium chlorite ($NaClO_2$), trimesoyl chloride (TMC), sodium chloride (NaCl), sulphuric acid (H_2SO_4), tetrahydrofuran (THF), dimethylformamide (DMF), α-bromoisobutyryl bromide (BiBB) (98 %), magnesium sulphate ($MgSO_4$), triethylamine (TEA, 99 %), 4-(Dimethylamino)pyridine (DMAP), copper(I) bromide (CuBr), glutamic acid (GLU), ethanol, polysulphone (PSF) pellets (MW = 35 000 g/mol), m-phenylenediamine (MPD), Methyl orange (MO), Methylene blue (MB) and Polyvinylpyrrolidone (PVP) (MW = 30–70 K; 87–90 %) were obtained from Sigma-Aldrich. By employing a Milli-Q system (Millipore), de-ionized (DI) water was produced with a resistivity of 18 mΩ cm. Hemp fibers were obtained locally.

2.2. Extraction of cellulose from cannabis sativa and CNC synthesis

The extraction of cellulose fibers was performed following a method reported by Mhlongo et al, 2022 [40]. To soften the bark, hemp branches and stems were immersed in water for a whole night then peeled from the woody core. The extracted bark was treated 4 wt% NaOH at 80℃ (2 h). This step was done three times to ensure complete delignification. The fibers were then bleached with a solution containing equal parts of acetate buffer (pH 4.8) and $NaClO_2$ (1.7 wt%) at 100℃ for 1 h, or till the fibers became white. Finally, the bleached fibers were rinsed with distilled water and air-dried.

3. Synthesis of cellulose nanocrystals from hemp cellulose fibers

Sulphuric acid (60 wt%) was added to bleached fibers. In summary, cellulose fibers were hydrolyzed with sulfuric acid (20 mL/g acid/pulp ratio). Dropwise, sulphuric acid was added with vigorous stirring while keeping the temperature below 30℃. The reaction mixture temperature was increased to 45 ℃ once the acid addition was finished. The reaction was kept at this temperature for an hour while being constantly stirred. The hydrolysis process was terminated by introducing 200 mL of cold water (about 2x the volume of acid solution). To obtain a precipitate, the diluted sample was centrifuged for 10 min at 11,000 rpm. After thorough agitation, the precipitate was re-suspended in water and centrifuged. This procedure was continued until the pH of the suspension reached 5, at which point dialysis was performed for three days to ensure that the pH remained constant. In order to disperse the nanocellulose in water, the suspension was sonicated using an ultrasonic homogenizer [41].

3.1. Synthesis of ATRP initiator grafted CNC (CNC-Br)

CNCs were modified by BIBB to prepare brominated CNCs (CNC-Br) prior to SI-ATRP reaction with glutamic acid. This was done following a

modified approach described by Zhang et al (2019) [42]. After sonicating the CNCs into the 50 mL of DMF, DMAP (2 g) and TEA (4 mL) were added. The suspension was stirred for 24 h after adding 4 mL of BIBB dropwise at 0 °C. The reaction was terminated with ethanol, rinsed with acetone 3 times, and dialyzed for 5 days in water. Finally, the CNC-Br was produced through freeze-drying.

3.2. Grafting GLU from CNC-Br by SI-ATRP

This was done following a comparable method described by Zhang et al (2017) [43]. In a typical reaction, CNC-Br was evenly dispersed in DMF using sonication and magnetic stirring. The mixture was then moved to a 250 mL round-bottom flask, where PMDETA and GLU monomer were introduced. These components were combined in a molar ratio of 100:1:1 for GLU, PMDETA, and CuBr. Before adding CuBr, the suspension was purged with nitrogen gas for 10 min. It was then degassed for an additional 10 min before being placed in an oil bath (70 °C) under magnetic stirring, allowing the reaction to proceed for 24 h. The reaction was concluded by exposing the mixture to air. To isolate CNC-GLU 100, the resulting mixture was washed with THF and ethanol, followed by centrifugation to eliminate any unreacted chemicals and free polymer, and finally freeze-dried.

3.3. Preparation of TFN membranes

Preparation of polysulfone (PSF) substrate.

The PSF support membrane was produced via the phase inversion method. To create the casting solution for the PSF membrane, a mixture consisting of 1 wt% PVP and 16 wt% PSF was dissolved in DMF solvent. This solution was stirred for 12 h at a temperature of 50 °C to ensure it was homogeneous. Following degassing, the solution was applied onto a glass plate to achieve a thickness of 100 μm, utilizing an Electrometer 4843 automatic film applicator from Manchester, UK. The coated plate was then submerged in a water coagulation bath at room temperature to enable solvent/non-solvent exchange through the wet phase inversion process. Afterward, the membrane film was thoroughly washed with fresh distilled water to eradicate any remaining DMF and was stored in distilled water until it was ready for use.

Preparation of polyamide (PA) selective layer.

The membranes PA layer was synthesized on a PSF support membrane using the traditional IP process. Pre-treatment of the PSF support membranes involved soaking them in an overnight solution (0.5 % sodium dodecyl sulphate (SDS)). Following that, distilled water was used to rinse the membranes for an hour. The substrate (PSF support) was subsequently secured between a frame and a glass plate. 2 w/v% MPD aqueous solution (20 mL) was poured onto the porous PSF substrate. After a 2-minute contact period, surplus MPD solution was removed from the sub-layer surface by placing it vertically (1 min). The PSF substrate was then contacted with the organic phase that contained 0.2 wt% TMC-hexane solution (1 min) before being removed from the membrane surface. Thereafter, the membrane was oven-dried for 8 min at 60℃ to increase crosslinking and washed with distilled water. The technique to fabricate CNC-GLU TFN membranes resembled that used for TFC membranes, with the exception that CNCs (modified) were first introduced to an aqueous solution of MPD (Table 1). Prior to affecting the interfacial polycondensation reaction, all MPD/additives solutions were sonicated for 30 min [44].

Table 1
TFN membranes CNC-GLU 100 loading.

Membrane	CNC-GLU 100 loading (wt%)
TFC	–
TFN	0.10

3.4. Characterization

The morphology of CNCs was analyzed with a FEI Tecnai G2 Spirit transmission electron microscope (TEM) (Hillsboro, USA) operating at an acceleration voltage of 120 kV. The Image J software was used to measure the diameter of CNCs. The chemical changes in CNCs and membranes were investigated using Fourier transform infrared (FTIR) spectroscopy, with spectra recorded between 4000 to 500 cm^{-1} using a Tensor 27 Infrared Spectrometer (Massachusetts, USA). X-ray diffraction (XRD) analysis was performed using a Bruker D2 Phaser diffractometer (Cu-Kα) (Johannesburg, South Africa) scanning from 5 to 90° (2θ), with a step size of 0.026 and a step time of 37 s. The solid-state ^{13}C nuclear magnetic resonance (^{13}C MAS NMR) spectra for CNC and CNC-GLU were obtained on an AVANCE-III-500 spectrometer (Bruker, Germany) using cross-polarization MAS with 4 mm zirconium rotors at a spin rate of 8 or 10 kHz. ^{13}C NMR chemical shifts were externally referenced to adamantane following Hoffman's method [45]. Elemental analysis of carbon, hydrogen, nitrogen, and sulfur (CHNS) was performed using a varioELcube v4.0.13 analyzer (Elementar, Germany). The thermal resistance of CNC and its derivatives was measured via thermogravimetric analysis (TGA), conducted with a thermogravimetric analyzer over a temperature range of 35–900 °C in a nitrogen atmosphere at a heating rate of 20 °C/ minute (Perkin Elmer). The surface and cross-sectional morphologies of the synthesized membranes were analyzed using field emission scanning electron microscopy (FESEM-EDS) (Carl Zeiss Sigma) at an accelerating voltage of 20 kV. Prior to imaging, the TFN membranes were coated with carbon and Pd/Au. Contact angle measurements were performed employing the sessile-drop method using a DataPhysics Optical Contact Angle apparatus (Germany). For each membrane sample, ten measurements were recorded at different locations.

CNC derivatives' pH point of zero charge (pH PZC) was ascertained using the salt titration method [45]. In short, 0.1 g of CNC-GLU 100 was added to five polypropylene tubes containing 25 mL of 0.01 M NaCl. The pH of these solutions was then adjusted between 2 and 10 with 0.1 M NaOH and 0.1 M HNO_3, giving each tube its own pH value. The suspensions were shaken horizontally for 24 h. The ultimate pH of each solution was plotted against the initial pH of the solutions, and the pH PZC for each material was computed using the intersection points [46].

3.5. Water uptake measurements

Water uptake of the TFN membranes was ascertained by measuring the change between their dry and wet weights. Membrane samples with an area of 0.00146 m^2 were first dried to remove moisture then weighed to determine their dry weight (W_d) before being immersed for 24 h in distilled water. After soaking, the membranes were lightly dabbed with paper to eliminate extra water, and then their wet weight (W_w) was measured (**Equation (1)**.

$$WIC(\%) = (W_w - W_d)/W_w X100 \quad (1)$$

3.6. Membrane performance

The efficacy of all fabricated membranes was assessed using a nitrogen-driven dead-end filtration system (Sterlitech, HP4750 Stirred Cell). Membrane samples (0.00146 m^2) were compacted with DI water under a transmembrane pressure of 600 kPa until a stable flux was reached. The pure water flux was then calculated at a pressure of 400 kPa using deionized water as the feed solution, following **Equation (2)**.

$$J_w = V/(A.\Delta t) \quad (2)$$

Where; J_w is the pure water flux ($L/m^2.h$),

4. Is the volume of the permeated water (L)

A is the effective area of the membrane (m^2),

Δt is the permeation time (h).

Salt and dye rejection tests were carried out on a dead-end filtration cell with continual magnetic stirring. Two organic dyes with varying electrostatic properties were used: methylene blue (MB) and methyl orange (MO) (Fig. 1). Various dye concentrations (20, 50, 80, and 100 mg/L) and pH were tested, and they were circulated through the cell at 400 kPa transmembrane pressure. The solute concentration was determined using UV–visible (UV–vis) spectroscopy. The feed also contained various salts (NaCl and $MgSO_4$) at concentrations of 2000 mg/L. Salts concentrations were detected by the conductivity meter (Hanna multimeter instrument, Hl 5522, South Africa).

The observed rejection (%R) was calculated using **Equation (3)**:

$$\%R = \left(1 - C_p/C_f\right)X100 \quad (3)$$

where C_p and C_f denote the dye concentrations (mg/L) of the feed and permeate solutions.

5. Results and discussion

5.1. Physiochemical characterization of CNC and derivatives

5.1.1. TEM analysis

By hydrolyzing hemp fibers with sulfuric acid, the CNCs used in this work were isolated, following a typical process published in the literature [41]. The morphology of CNCs and its derivatives was visualized using TEM (Fig. 2). Synthesized CNCs were rod-shape with a mean diameter of 4.9 ± 1.6 nm. The CNCs exhibits laterally aggregated rods due of its large specific area and strong hydrogen bonding between nanocrystals [47]. Upon attachment with the initiator, the CNCs still maintained a rod-shaped morphology with no change in diameter (Fig. 2 **(b, b')**). EDS analysis of CNC-Br was carried out (Fig. S1). The EDS analysis of CNC-Br confirmed the presence of Br, C, and O at 1.48, 0.26, and 0.51 keV respectively, verifying the attachment of the Br containing initiator to the CNC.

However, growing glutamic acid chains on the surface of the CNCs exhibits an opaque layer around the CNCs, with an increase in diameter (9.4 ± 1.7 nm) (Fig. 2 **(c, c')**). The difference in the structural integrity prior to and following grafting modification could be used to indicate the presence of GLU brushes [48]. Kiriakou et al. (2021) observed comparable results in their study, wherein CNCs were grafted with Poly (butyl acrylate) synthesized in either toluene or DMF, along with a free polymer derived from a sacrificial initiator [49]. The initiator-attached CNCs maintained their rod-shaped structure and resembled their unaltered precursors according to TEM imaging, while the DMF polymerized CNCs displayed increased width but similar lengths, which was consistent with polymer grafting [49].

5.1.2. FTIR, XRD, CP/MAS ^{13}C NMR, CHNS, TGA, PZC analysis

The CNCs and derivatives were characterized using FTIR, XRD, CP/MAS ^{13}C NMR, CHNS and pH PZC as depicted in Fig. 3. The FTIR spectroscopy revealed the effective grafting of the BIBB initiator on the surface of CNCs. Fig. 3**(a)** displays the spectra of pure CNCs, CNC-Br and CNC-GLU 100. The CNC spectrum exhibits significant bands at 3319 cm^{-1} ascribed to the O–H groups. The bands at 2897, 1368 and 1640 cm^{-1} are due to the C–H stretching and bending, and carboxyl groups stretching vibrations, respectively. Compared to the CNC, CNC-Br samples revealed an additional FTIR peak at around 1724 cm^{-1} owing to the ester carbonyl group of ATRP initiator attached to the CNCs [50,51]. There was a decrease in peak at 3319 cm^{-1} after ATRP initiator attachment, indicating that some surface O–H groups were replaced [52]. Upon growing the glutamic acid brushes on CNCs, the spectra displayed peaks at 1728 cm^{-1} allotted to the stretching vibration of −C=O bond due to the presence of the carboxylic group in glutamic acid. The peaks at 1570, 1371 and 1131 cm^{-1} are ascribed to the N–H bend, −C-N- stretching in the secondary amide groups, respectively suggesting that amidation reaction was successful.

XRD analysis was used to explore alterations in the crystalline structure of CNCs after acidic hydrolysis, esterification with BIBB, and polymerization with glutamic acid (Fig. 3 **(b)**). The CNC diffractograms exhibited a broad amorphous hump with distinct crystalline peaks, characteristic of a semi-crystalline material. Three crystalline peaks typical of cellulose I were present at approximately 2θ = 15.5°,16.5° (110), 22.7° (002) and 34.6° (004) [53,54]. Upon attachment with BIBB initiator, there was no observable difference in the pattern suggesting that the CNCs maintained their structure during the reaction. The XRD pattern for glutamic acid demonstrated the high crystallization imparted on the CNC-GLU 100 following its polymer growth on CNCs.

The thermal resistance of CNC and derivatives was investigated by means of TGA analysis as shown in Fig. 3**(c)**. The pure CNCs thermogram correlates with the thermal behavior commonly detected for CNCs produced by sulfuric acid hydrolysis [55]. The minor weight loss observed below 150°C is due to the absorbed moisture content of the samples. The CNCs exhibited major weight loss at 210–430°C due to cellulose chain degradation which includes dehydration, depolymerization, and decomposition of glycosidic units. CNC-Br showed a similar weight loss pattern, however it exhibited its main loss between 182 and 400°C. The CNC-Br exhibited lower thermal stability due to the labile bromine, upon heating it forms HBr which can speed the degradation of cellulose [56,57]. Upon grafting the CNC-Br with glutamic acid brushes, there was an increase in Tonset (~180°C), and the main weight loss step shifted to 194–362 °C. This was due to the presence of glutamic acid chains that minimize exposure to high temperature thus increasing resistance to thermal degradation.

The pH at which a material has zero net surface charge in a particular solution is referred to as its PZC [58]. It was observed that the pH PZC of CNC-GLU 100 was 5.13, this implies that at pHs lower than 5.13 the surface charge is positive, neutral at 5.13 and negatively charged at higher pHs (Fig. 3**(d)**) [59]. Adding CNC-GLU 100 to the PA layer of TFN membranes unavoidably impacts their overall charge. This might suggest that the membrane's PZC pH might be close to 5.13.

The elemental analysis also revealed the contents of C, H, N and S

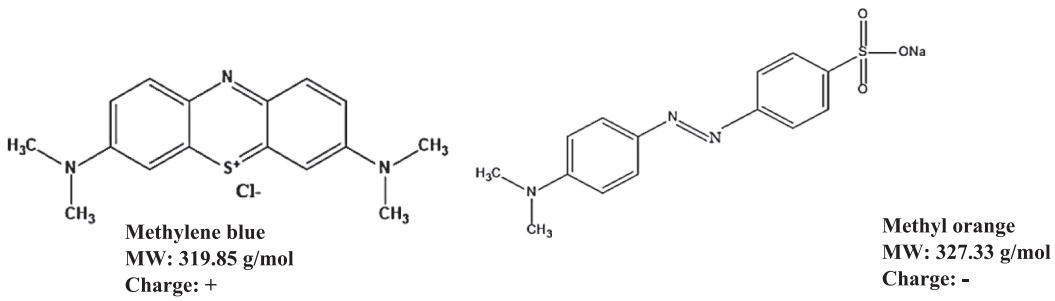

Fig. 1. The molecular structure, weight and charge of the dyes.

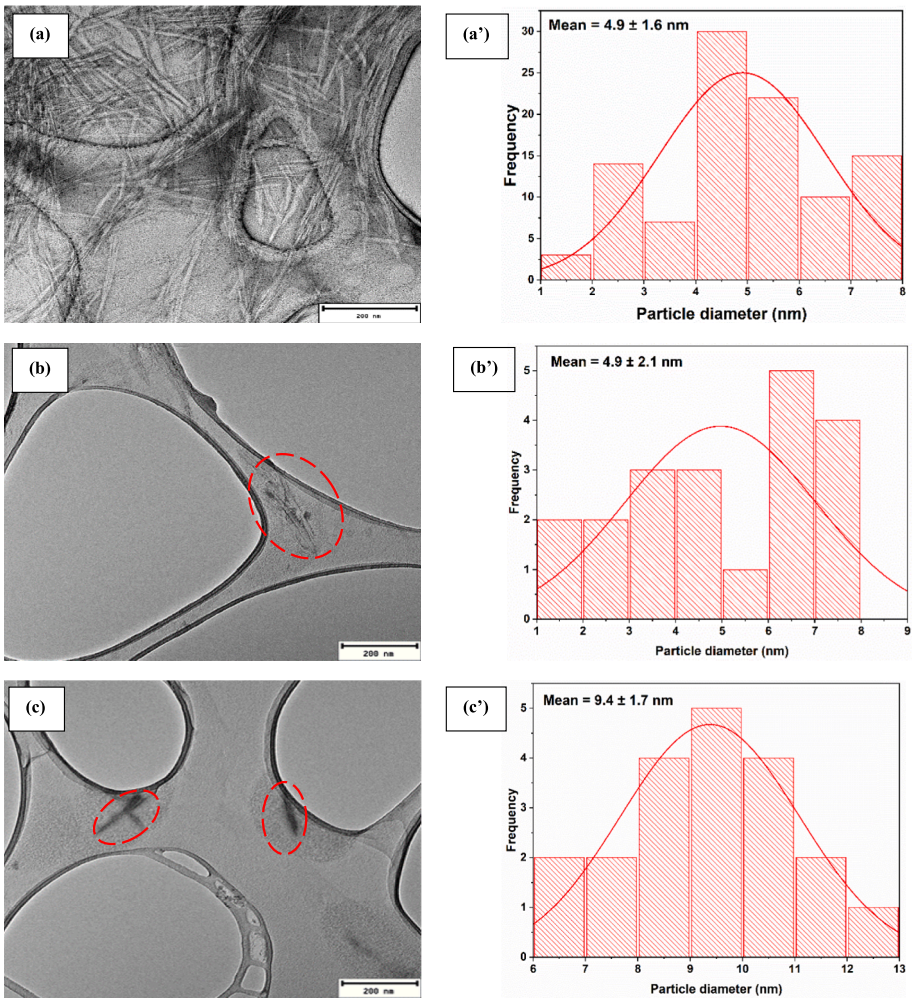

Fig. 2. TEM image of pristine CNC, CNC-Br and CNC-GLU 100 (a – c), and corresponding size distribution histogram (a'–c').

present in the CNC and derivatives as shown in Table 2. The Nitrogen content increased with the grafting of the glutamic acid brushes (0.54–2.76 %). This correlates with the TEM analysis where a dense layer is observed around CNCs after growing glutamic acid brushes.

The high-resolution ^{13}C CP/MAS NMR spectrum of GLU confirms the presence of both α and β polymorphs, with all signals clearly resolved (Fig. 4). This is consistent with the chemical shifts reported by Wang and colleagues [60]. After grafting GLU onto CNC, the signals from GLU broaden, as expected for polymerised GLU on the CNC surface (Fig. 4). No significant changes in the peak width or chemical shift of the CNC were observed, suggesting that the structure of the CNC is largely preserved, corroborating our findings from other characterisation techniques.

5.2. *Characterization of CNC-GLU -functionalized TFN membranes*

5.2.1. *Morphology of TFN membranes*

The membranes surface and cross-section morphologies were characterized with FESEM and AFM imaging as depicted in Fig. 5. The TFC membrane exhibits spherical globules and rough nodules credited to the crosslinking in between MPD and TMC (Fig. 5 **(a)**). This also shows that the PA layer completely covers the substrate layer [34]. This typical ridge valley structure is observed in polyamide layers prepared via interfacial polymerization [31]. However, upon CNC-GLU 100 incorporation, more leaf-like nodules are observed (Fig. 5 **(b)**). This might have occurred owing to the presence of hydrophilic CNCs, which can facilitate the IP procedure by improving the compatible mixing of the aqueous and organic phases and the diffusion of MPD into the organic phase [30,61]. Shamar et al (2022) noted similar findings after the formation of PA layer with Co-Zn based mixed metal–organic frameworks (mMOFs) incorporated in MPD and TMC [62]. Both TFC and TFN membrane after diffusion reaction of monomers (TMC and MPD) exhibited a typical ring and leaf shape structure. However, a prominent leaf-like structure was observed in TFN membrane, this is due to the occurrence of highly porous evenly distributed mMOFs. This results in improved containment of gases (resultant CO_2 gasses that are IP by-products trapped in PA layer resulting in ridge valley morphology), therefore a leaf-like PA formation is favored [62]. Furthermore, Fig. S2 demonstrates the successful formation of a PA layer atop the PSF substrate for both TFC and CNC-GLU TFN membranes as indicated by the visible PA layer.

The surface roughness analysis is presented in Fig. 5 **(a')** and **(b')**. As illustrated, the architecture of the membrane surfaces appears in the form of dark and light areas illustrating valleys and peaks, respectively. The TFC membrane exhibited a greater surface roughness (Sa = 103 nm) than the TFN membrane (Sa = 63 nm). This is likely caused by the formation of hydrogen bonds in between CNCs and MPD coupled with the presence of hydroxyl and polar functional groups of the CNC-GLU which can hinder the formation of the PA layer thus causing the membrane to smoothen [63]. In theory, membrane surfaces with low roughness and high hydrophilicity have the potential to provide improved fouling resistance [64]. The change in both morphology and surface roughness proves the proper dispersion and distribution of CNC-GLU 100 embedded in the PA layer.

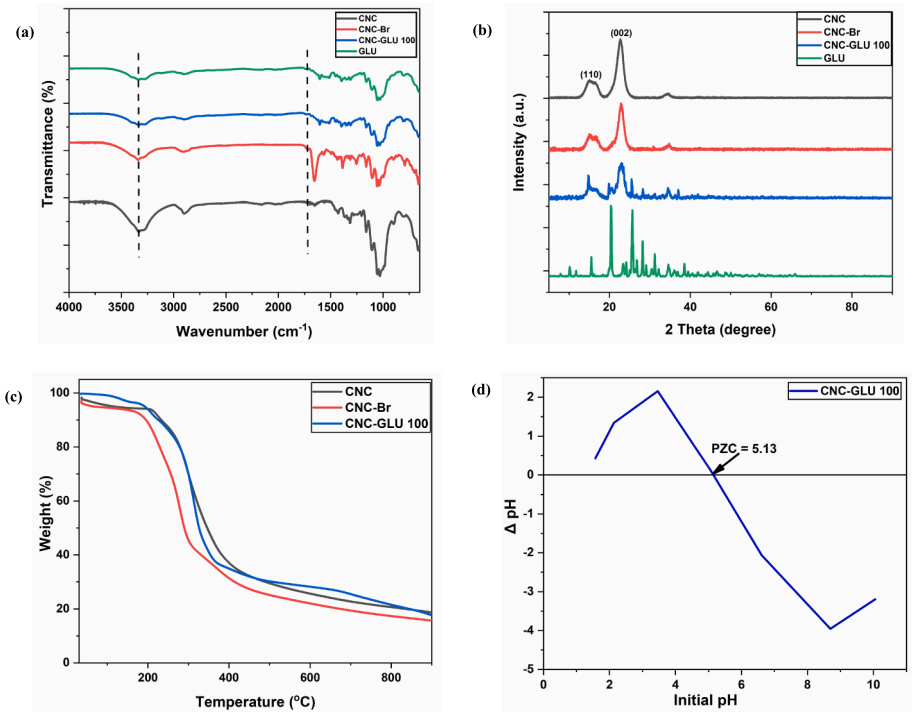

Fig. 3. FTIR spectra (a), TGA thermograph (b), XRD patterns (c) and PZC (d) of CNC, CNC-Br, CNC-GLU 100.

Table 2
Elemental analysis of CNC, CNC-GLU 100 and GLU.

Sample	C (%)	H (%)	N (%)	S (%)
CNC	35.76	4.348	0.54	0.185
CNC-Br	42.29	5.791	0.15	0.319
CNC-GLU 100	37.13	5.221	2.76	0.036
GLU	32.18	4.974	7.57	0

5.2.2. *FTIR of membranes*

The surface functional groups of PSF, TFC and CNC-GLU TFN membranes were analyzed using FTIR as illustrated in Fig. 6. The pure PSF membrane exhibited distinctive peaks at 1322, 1293, 1489, and 2981 cm^{-1} which are corresponding to the following molecular vibrations: asymmetric stretching of C-SO_2-C, S=O stretching, C=C stretching present in the aromatic ring and aliphatic C–H stretching respectively [65]. The peaks at 828 and 1007 cm^{-1} are ascribed to the aromatic rocking vibrations of the C–H bonds. Upon the formation of the active PA layer on the PSF, different spectra is observed for both TFC and TFN membrane. The appearance of the peak at 1658 cm^{-1} is ascribed to the reaction between the acryl chloride groups of TMC and the amine groups found in MPD solution [66]. The peak at 1542 cm^{-1} relates to N–H bending and C-N stretching vibrations associated with the amide II band. These peaks confirm the successful synthesis of the polyamide layer via IP [32,66]. Regardless of the CNC incorporation, both TFC and TFN display similar spectra with noteworthy peaks at 1658, 1241 cm^{-1} which are credited to C=O (Amide I) and C-N stretch [67]. Furthermore, TFN exhibits a broad band at 3372 cm^{-1} ascribed to the O–H stretching from the partially hydrolyzed acyl chloride of TMC and the CNC-GLU 100 [68,69].

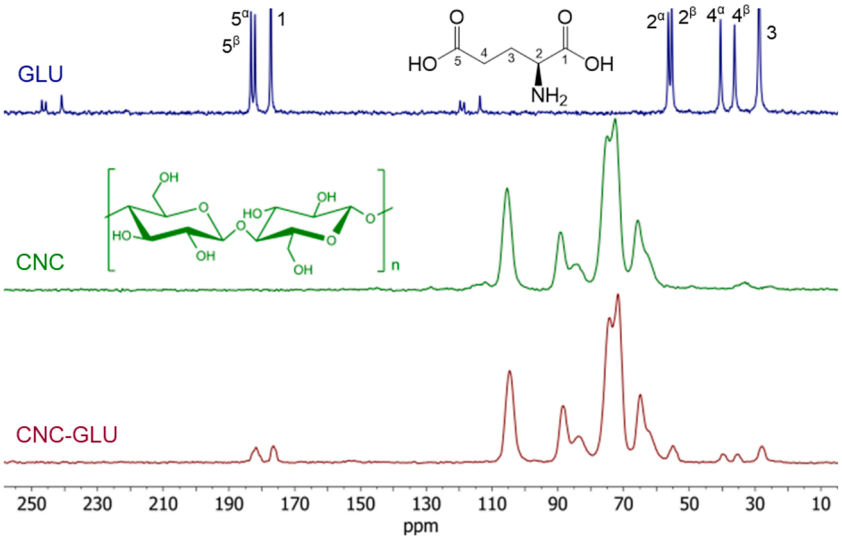

Fig. 4. 13C CP/MAS NMR spectrum of CNC, GLU, and CNC-GLU 100 (Pulse program: CP/MAS; MAS rate: 8–10 kHz).

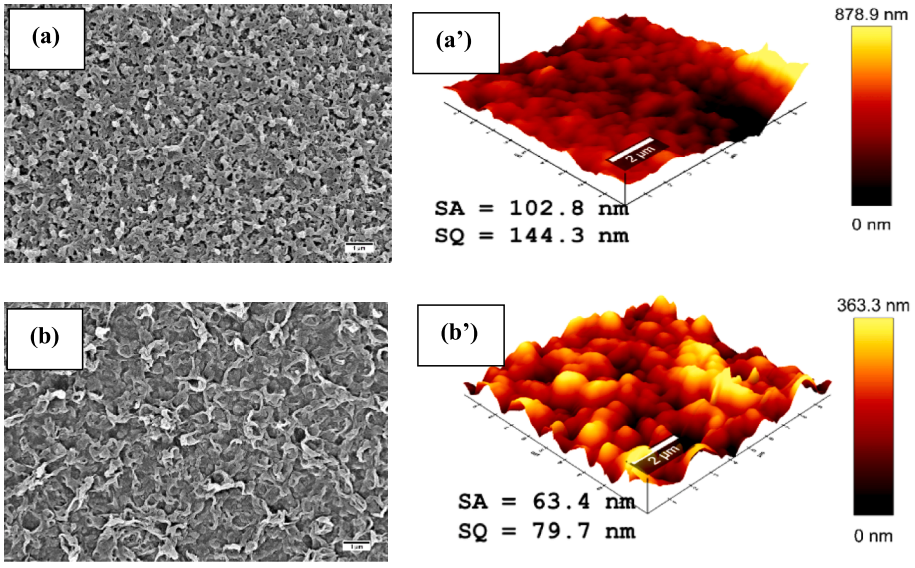

Fig. 5. Surface (a, b), and AFM images (a', b') of TFC and CNC-GLU TFN membranes.

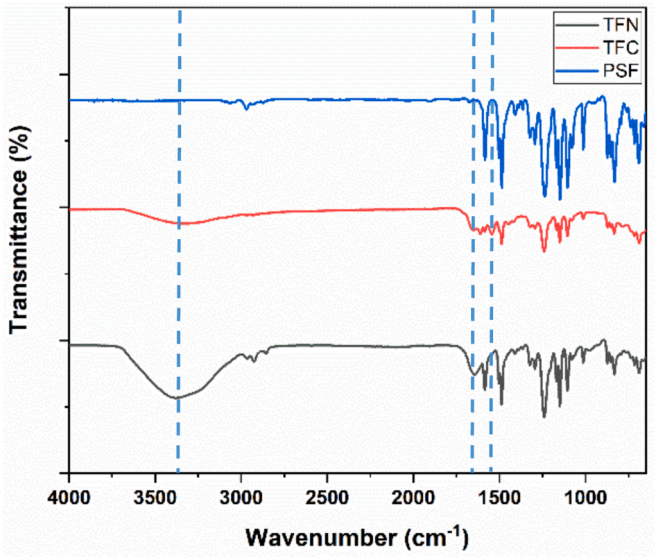

Fig. 6. FTIR spectra for PSF, TFC and CNC-GLU TFN membrane.

5.2.3. Water permeability studies

The hydrophilicity of the TFC and CNC-GLU TFN membranes was assessed using water intake capacity (WIC) and contact angle measurements (Table 3). The swelling capacity or WIC of a membrane is a measurement of its bulk hydrophilicity. The WIC increased upon the addition of CNC-GLU 100 into the PA layer. The TFN membrane exhibited a higher WIC (70.63 %) as opposed to the TFC membrane (59.62 %). These results correlated with the contact angle measurements whereby TFN membrane proved to be more hydrophilic by exhibiting a lower CA (76 ± 4°) as compared to the TFC membrane (95 ± 2°). The CNC-GLU 100 enhanced the hydrophilicity of the membranes due to the presence of hydrophilic carboxyl and hydroxyl groups [70,71]. The increase in hydrophilicity suggests an increased water flux and antifouling properties [71].

Table 3
Membrane pure water permeation studies.

Membrane	WIC (%)	WCA (°)
TFC	59.62	95 ± 2
CNC-GLU TFN	70.63	76 ± 4

5.3. Membrane performance

5.3.1. Pure water flux

Fig. 7 demonstrates the pure water flux of the TFC and CNC-GLU TFN membranes at 400 kPa. Upon the introduction of CNC-GLU 100 into the PA layer, there was an observable increase in permeate water flux from 7.11 ± 0.63–15.45 ± 1.03 L/m^{2}h. The inclusion of CNC-GLU 100 into the PA layer dramatically enhances pure water flux owing to the rise in hydrophilicity resulting from the addition of hydrophilic groups to the polyamide film [29]. The CNC-GLU 100 exhibits a high surface density of functional groups, including hydroxyl, carboxyl, and amine moieties, which confer a hydrophilic nature to the membrane. The enhanced surface area of CNC-GLU 100, coupled with the electrostatic effects arising from functionalization, led to an increase in membrane flux. Moreover, the free volume created by the restricted phase separation stemming from the tight interfacial bonding between functionalized CNCs and the polyamide matrix mimics water conduits, thus boosting

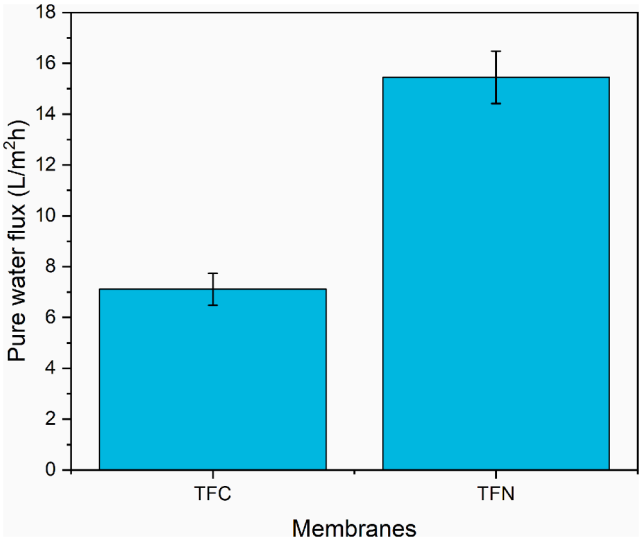

Fig. 7. Pure water flux for TFC and CNC-GLU TFN membranes.

water transport efficiency.

5.3.2. Membrane separation performance

5.3.2.1. Influence of dye concentration and pH on removal capacity. The separation efficiency of the membranes for the rejection of dyes was assessed by varying both the dye concentrations and pHs of MO and MB. The concentration of the dyes ranged from 20–100 mg/L as shown in Fig. 8. The TFC membrane rejection of MB dye ranged from 83.63–96.29 %, whilst CNC-GLU TFN rejection ranged from 93.91 – 99.83 %. MO dye rejections were lower for both TFC (54.83–60.16 %) and TFN (74.15–90.63 %). These results demonstrate that the inclusion of modified CNC enhances dye separation by increasing the electrostatic charge of the membrane. The rejection behavior can be due to sieving, steric hindrances and the Donnan exclusion principle [72]. MB's enhanced rejection can be ascribed to its larger hydrated radii of 5.04A as compared to MOs radii of 4.97A, which produces sieving hindrances [73,74]. The abundance of carboxyl groups on the glutamic acid modified CNCs in the TFN membrane generates a negative surface charge causing the membrane to have substantial electrostatic attraction to MB. Conversely, electrostatic repulsion towards the anionic MO dye is caused by the membrane's negatively charged surface thus improved rejection was observed for the cationic MB dye. Fig. 9 reveals that dye solutions (50 mg/L) showed lower permeate fluxes than pure water due to dye adsorption on membrane surfaces.

Fig. 9 further indicates that the dye flux is higher in MB than in MO. The incorporation of negatively charged CNC-GLU 100 imparts a negative surface charge. As a result, this surface is likely to repel anionic dyes more effectively than cationic dyes, leading to a decrease in the flux of anionic dyes due to electrostatic repulsion. Conversely, cationic dyes may encounter less repulsion or even electrostatic attraction, resulting in an increased flux.

pH studies were carried out at pH 2, 6.5, and 11 using dye filtration with TFC and TFN membranes, with results shown in Fig. 10 **(a)** and **(b)** for MB and MO, respectively. Given that solution pH has a direct impact on the electrochemical attributes of the dye molecules and membrane surface, membrane separation efficiency can be successfully regulated. At all pH ranges, the rejection rate of MB was greater than 85 %, with rejection increasing to 96 % at pH levels above 7. At lower pH levels, the negative charge on the membrane surface weakens, making it easier for negatively charged MO molecules to adsorb and deposit. At pH 2, MO had the highest rejection rate (~90 %). A decrease in MO rejection is caused by an increase in the membranes surface negative charge when the pH of the solution rises. Electrostatic repulsion hindered the ability of negatively charged MO dye molecules to adsorb on the membrane surface.

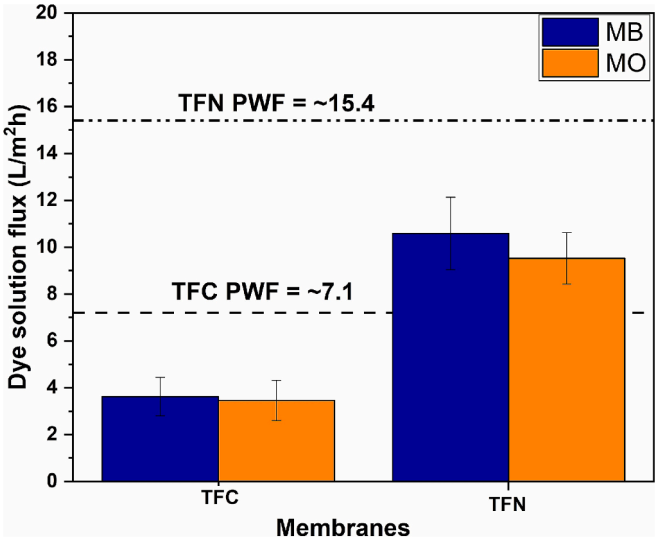

Fig. 9. Dye solution flux for TFC and CNC-GLU TFN membranes.

5.3.3. Membrane recyclability and long-term performance studies

Membrane reusability is crucial for practical applications, especially on a large scale; hence, membrane effectiveness and durability are critical. Even after six cycles (30 min per cycle), Fig. 11 shows that the CNC-GLU TFN membrane demonstrated outstanding rejection ability for both MB and MO dyes (50 mg/L, solution pH). After six cycles, both dyes showed a decline in their removal efficiency. MB dye removal effectiveness reduced from 97.98 to 88.26 % whilst MO rejection decreased from 88.97 to 79.98 %. This could be explained by membrane fouling or the cleaning process's failure to eliminate absorbed dye molecules. This will eventually lead to a reduction in the membrane's removal efficacy.

5.3.4. Long-term performance studies

The long-term operational durability of the CNC-GLU TFN membrane was also assessed. The normalized permeate flux and dye rejection performance of the CNC-GLU TFN membrane when filtering a 50 mg/L MB solution at 400 kPa are illustrated in Fig. 12. The CNC-GLU TFN membrane retained a dye rejection above 99 % during continuous operation spanning over 400 min. However, its permeate flux toward MB exhibited a gradual decline over time. This performance degradation was linked to progressive fouling mechanisms, including the formation of a dense cake layer on the membrane surface and associated pore occlusion. These factors contributed to increased concentration polarization effects, ultimately reducing membrane permeability.

An examination of macro- and microscopic images of the CNC-GLU TFN membranes (Fig. 13) revealed the extent of fouling during

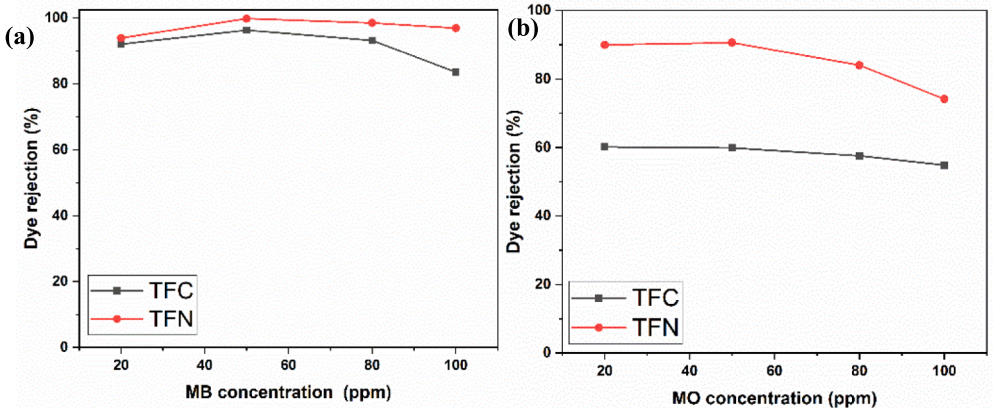

Fig. 8. Dye rejection performance of TFC and CNC-GLU TFN membranes; MB (a) and MO (b).

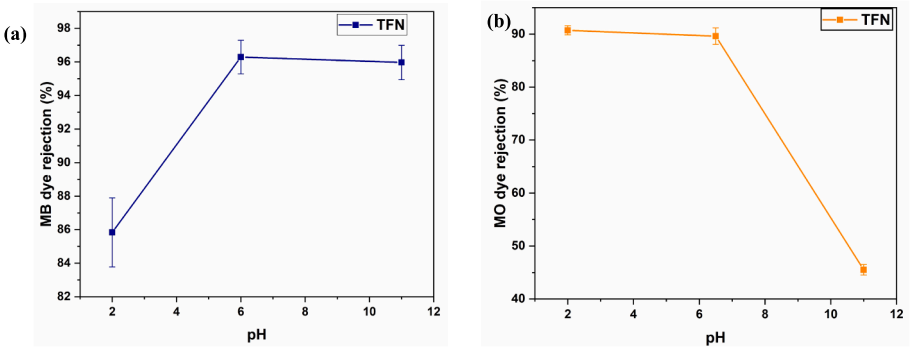

Fig. 10. TFN dye rejection vs pH; MB (a) and MO (b).

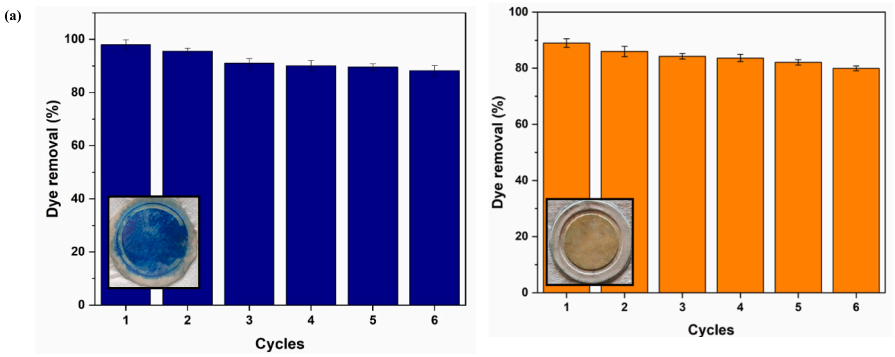

Fig. 11. The cycles of reusability for CNC-GLU TFN; MB (a) and MO (b). (Insert: Photos of CNC-GLU TFN after filtration cycles).

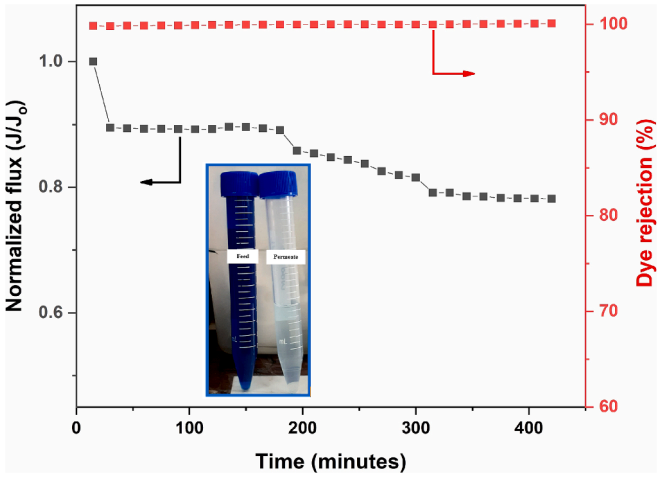

Fig. 12. Long-term performance studies for CNC-GLU TFN membrane (Insert: Digital photographs of the feed and the permeate).

membrane filtration. After > 400 min of filtration with MB dye at a concentration of 50 mg/L, the membrane surface was fully covered by dye molecules. The impact of this fouling was evident in the decline of filtrate flux over time, which compromised the overall filtration performance. This phenomenon is likely influenced by multiple factors, including the formation of a cake layer, adsorptive fouling, and pore blockage. These mechanisms can modify the membrane's characteristics, leading to increased resistance during filtration.

5.4. Dye removal from spiked river water

River water samples from South Africa's Vaal River were spiked (50 mg/L) and tested for the prospective utilization of these membranes in environmental water bodies. The water samples had the following physicochemical characteristics: conductivity 834 μS/cm, pH 7.61, resistivity 1.20 KΩ.cm and total dissolved solids (TDS) 417 ppm. The TFN membrane exhibited higher removal efficiency for both MB (99.26 %) and MO (82.62 %) dyes than the control TFC membrane, which removed 94.56 and 49.85 % for MB and MO, respectively. The increased removal observed for the TFN is due to the synergistic elimination caused by steric hindrance effects, sieving, and Donnan exclusion [72].

5.5. Salt removal studies

In addition to dye removal studies, salt rejection was also examined. In a single component system, the rejection of NaCl and $MgSO_4$ was studied using a TFN membrane. The rejection of salts was found to be greater for $MgSO_4$ than for NaCl, as depicted in Fig. 14. This aligns with the typical behavior of negatively charged nanofiltration (NF) membranes, as reported in the literature [25,75,76]. Overall, the rejection performance is influenced by both size exclusion and the Donnan exclusion effect. The enhanced rejection of sulfate ions compared to chloride ions is primarily due to the larger hydrated radius and higher charge of SO_4^{2-} (0.38 nm) relative to Cl^- (0.33 nm) [77]. Furthermore, the divalent cation Mg^{2+} has a more significant impact on the negatively charged membrane surface compared to Na^+. As a result, $MgSO_4$ exhibits a higher rejection rate than NaCl.

5.6. Performance comparison to other reports

Table 4 presents a comparison of TFN membrane performance in terms of dye rejection and permeability, specifically contrasting them with those developed in this research. The CNC-GLU TFN membranes exhibited a good water flow and comparable dye rejection capabilities at low operating pressures. In contrast, most NF membranes typically function at significantly higher pressures, which substantially increases

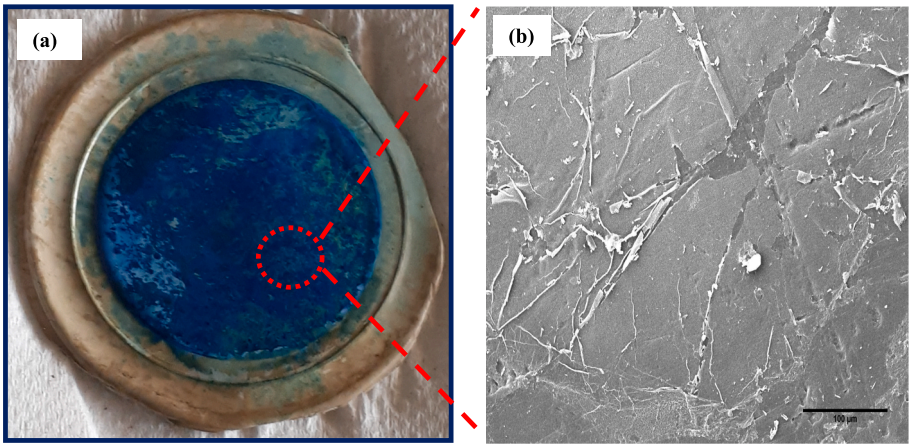

Fig. 13. Digital photograph (a) and SEM image (b) of fouled CNC-GLU TFN membrane after long-term filtration studies with MB dye (50 mg/L; 420 min).

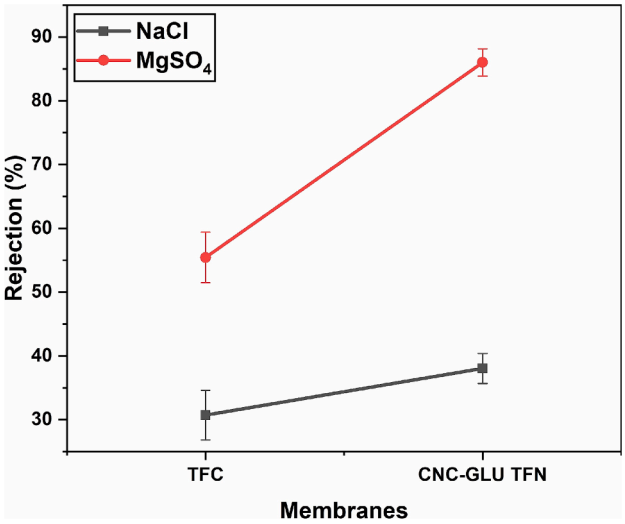

Fig. 14. Salt rejection of the synthesized TFC and TFN membranes (the test conditions: P = 400 kPa, C_f = 2000 mg/L).

operational costs. The impressive separation efficacy of CNC-GLU TFN membranes under reduced pressure conditions suggests that cellulose nanocrystals (CNCs) serve as effective filler materials for the creation of low-pressure TFN NF membranes.

6. Conclusion

Utilizing interfacial polymerization (IP), TFN membranes containing glutamic acid-modified cellulose nanocrystals (CNC-GLUs) were developed in this study. CNCs were synthesized from hemp fibers, and glutamic acid brushes were grown through SI-ATRP. These modified CNCs were characterized using a series of characterization tests (XRD, CP/MAS ^{13}C NMR spectroscopy, CHNS, TEM, and FTIR). Subsequently, varying ratios of CNC-GLUs, specifically 0 wt% (TFC) and 0.10 wt% (CNC-GLU TFN), were added to the aqueous phase during membrane construction. Given that the CNCs added hydrophilic groups to the polyamide film, the hydrophilicity of the PA layer significantly improved. The TFN membrane exhibited the highest PWF (15.45 ± 1.03 L/m^{2}h) and a lower contact angle (76 ± 4°). TFN membranes also demonstrated outstanding rejection of both MB and MO dyes from water, as well as the ability to reject these dyes from environmental water samples (99.26 % and 82.62 %, respectively). The TFN membranes further displayed enhanced salt rejection making it a capable choice in wastewater treatment. The improved membrane performance and durability of these CNC-GLU TFN membranes is promising for dye removal applications and other industrial separation processes since CNCs are environmentally friendly, produced from sustainable materials, and modification using SI-ATRP is a straightforward procedure.

CRediT authorship contribution statement

Khona Maziya: Conceptualization, Methodology, Validation, Investigation, Writing – review & editing. **Izak Kotze:** Methodology, Validation, Investigation, Writing – original draft. **Oranso T. Mahlangu:** Methodology, Investigation. **Heidi Lynn Richards:** Conceptualization, Resources, Writing – review & editing, Project administration.

Declaration of competing interest

The authors declare that they have no known competing financial interests or personal relationships that could have appeared to influence

Table 4
Comparison of Dye Separation Performance between CNC-GLU TFN and existing Studies.

Membrane	Types of dyes	Permeability	Dye rejection (%)	Pressure (Bar)	References
TFN (CNQDs 0.08 wt%)	Methyl Blue	13.8 $Lm^{-2}h^{-1}bar^{-1}$	96.1	5	[78]
TFN (UiO-66-NH_2 0.02 wt%)	Malachite green (MG)	13.32 ± 0.6 $Lm^{-2}h^{-1}$	91.90 ± 3	10	[79]
TFN (GO-TiO_2-Ag 0.2 wt%)	Rose bengal	52 $Lm^{-2}h^{-1}$	98	7	[75]
TFN (HNT 0.04 wt%)	Setazol red	~28 $Lm^{-2}h^{-1}$	99.7	9	[25]
	Reactive orange		99.7		
TFN (polydopamine modified CNCs)	Congo red/NaCl	128.4 $Lm^{-2}h^{-1}bar^{-1}$	99.91	2	[76]
TFN-1 (MOFs)	Rhodamine B	20.6 $Lm^{-2}h^{-1}bar^{-1}$	99.9	4	[80]
TFN (COFs-polyester)	Congo red	105 $Lm^{-2}h^{-1}bar^{-1}$	98.5	2	[81]
TFN (CNF-CNTs/ZIF-67)	Methyl blue	207.8 $Lm^{-2}h^{-1}bar^{-1}$	95.1	1	[82]
TFN (CNC-GLU 100)	MB	15.4 $Lm^{-2}h^{-1}$	99.83	4	**This study**
	MO		90.63		

the work reported in this paper.

Appendix A. Supplementary data

Supplementary data to this article can be found online at https://doi.org/10.1016/j.seppur.2025.132829

Data availability

Data will be made available on request.

References

[1] E. Forgacs, T. Cserháti, G. Oros, Removal of synthetic dyes from wastewaters: A review, *Environ Int.* 30 (7) (2004) 953–971, https://doi.org/10.1016/j.envint.2004.02.001.

[2] G. Zeng, Z. Ye, Y. He, X. Yang, J. Mang, H. Shi, Z. Feng, Application of dopamine-modified halloysite nanotubes/PVDF blend membranes for direct dyes removal from wastewater, *Chem Eng J.* 323 (2017) 572–583, https://doi.org/10.1016/j.cej.2017.04.131.

[3] N. Gowriboy, R. Kalaivizhi, M.R. Ganesh, K.A. Aswathy, Development of thin film polymer nanocomposite membrane (ZIF-8@PSf/CS) for removal of textile pollutant and evaluating the effect of water samples on human monocytic cell lines (THP-1) using flow cytometer, *J Clean Prod.* 377 (2022) 134399, https://doi.org/10.1016/j.jclepro.2022.134399.

[4] L. Xu, L.S. Du, C. Wang, W. Xu, Nanofiltration coupled with electrolytic oxidation in treating simulated dye wastewater, *J Memb Sci.* 409–410 (2012) 329–334, https://doi.org/10.1016/j.memsci.2012.04.001.

[5] J. Meng, Y. Xie, Y.H. Gu, X. Yan, Y. Chen, X.J. Guo, W.Z. Lang, PVDF-CaAlg nanofiltration membranes with dual thin-film-composite (TFC) structure and high permeation flux for dye removal, *Sep Purif Technol.* 255 (2021) 117739, https://doi.org/10.1016/j.seppur.2020.117739.

[6] L.A.V. de Luna, T.H.G. da Silva, R.F.P. Nogueira, F. Kummrow, G.A. Umbuzeiro, Aquatic toxicity of dyes before and after photo-Fenton treatment, *J Hazard Mater.* 276 (2014) 332–338, https://doi.org/10.1016/j.jhazmat.2014.05.047.

[7] M. Punzi, F. Nilsson, A. Anbalagan, A. Anbalagan, B.M. Svensson, K. Jönsson, B. Mattiasson, M. Jonstrup, Combined anaerobic-ozonation process for treatment of textile wastewater: Removal of acute toxicity and mutagenicity, *J Hazard Mater.* 292 (2015) 52–60, https://doi.org/10.1016/j.jhazmat.2015.03.018.

[8] W. Yu, Y. Liu, Y. Xu, R. Li, J. Chen, B.Q. Liao, L. Shen, H. Lin, A conductive PVDF-Ni membrane with superior rejection, permeance and antifouling ability via electric assisted in-situ aeration for dye separation, *J Memb Sci.* 581 (2019) 401–412, https://doi.org/10.1016/j.memsci.2019.03.083.

[9] M.A. Halakarni, V. Polisetti, A.A. Samage, A. Mahto, A.J. Svagan, M.S. Hedenqvist, S.K. Nataraj, Design of selective and self-cleaning iron aminoclay thin film nanocomposite membranes, *Chem Eng J.* 456 (2023) 140941, https://doi.org/10.1016/j.cej.2022.140941.

[10] S. Mohammad Nejad, S.F. Seyedpour, S. Aghapour Aktij, M. Dadashi Firouzjaei, M. Elliott, A. Tiraferri, R.A. SadrzadehM, Loose nanofiltration membranes functionalized with in situ-synthesized metal organic framework for water treatment, *Mater Today Chem.* 24 (2022) 100909, https://doi.org/10.1016/j.mtchem.2022.100909.

[11] P. Karami, S.A. Aktij, B. Khorshidi, M.D. Firouzjaei, A. Asad, M. Elliott, A. Rahimpour, J.B.P. Soares, M. Sadrzadeh, Nanodiamond-decorated thin film composite membranes with antifouling and antibacterial properties, *Desalination.* 522 (2022) 115436, https://doi.org/10.1016/j.desal.2021.115436.

[12] M.D. Firouzjaei, S.F. Seyedpour, S.A. Aktij, M. Giagnorio, N. Bazrafshan, A. Mollahosseini, F. Samadi, S. Ahmadalipour, F.D. Firouzjaei, M.R. Esfahani, A. Tiraferri, M. Elliott, M. Sangermano, A. Abdelrasoul, J.R. McCutcheon, M. Sadrzadeh, A.R. Esfahani, A. Rahimpour, Recent advances in functionalized polymer membranes for biofouling control and mitigation in forward osmosis, *J Memb Sci.* 596 (2020) 117604, https://doi.org/10.1016/j.memsci.2019.117604.

[13] A.F. Ismail, P.S. Goh, S.M. Sanip, M. Aziz, Transport and separation properties of carbon nanotube-mixed matrix membrane, *Sep Purif Technol.* 70 (1) (2009) 12–26, https://doi.org/10.1016/j.seppur.2009.09.002.

[14] Y. Rahimi-Kashkouli, M. Rahbari-Sisakht, A.G.J. Ghadam, Thin film nanocomposite nanofiltration membrane incorporated with cellulose nanocrystals with superior anti-organic fouling affinity, Environ Sci Water Res Technol 6 (3) (2020) 715–723, https://doi.org/10.1039/c9ew00963a.

[15] P. Zhao, R. Li, W. Wu, J. Wang, J. Liu, Y. Zhang, In-situ growth of polyvinylpyrrolidone modified Zr-MOFs thin-film nanocomposite (TFN) for efficient dyes removal, *Compos Part B Eng.* 176 (2019) 107208, https://doi.org/10.1016/j.compositesb.2019.107208.

[16] Y. Mansourpanah, A. Ghanbari, H. Yazdani, G.A. Mohammadi, A. Rahimpour, Silver-polyamidoamine/graphene oxide thin film nanofiltration membrane with improved antifouling and antibacterial properties for water purification and desalination, *Desalination.* 511 (2021) 115109, https://doi.org/10.1016/j.desal.2021.115109.

[17] D.L. Zhao, H. Jin, Q. Zhao, Y. Xu, L. Shen, H. Lin, T.-S. Chung, Smart integration of MOFs and CQDs to fabricate defect-free and self-cleaning TFN membranes for dye removal, *J Memb Sci.* 679 (2023) 121706, https://doi.org/10.1016/j.memsci.2023.121706.

[18] S.R. Mousavi, M. Asghari, N.M. Mahmoodi, Chitosan-wrapped multiwalled carbon nanotube as filler within PEBA thin film nanocomposite (TFN) membrane to improve dye removal, *Carbohydr Polym.* 237 (2020) 116128, https://doi.org/10.1016/j.carbpol.2020.116128.

[19] N. Ghaemi, P. Safari, Nano-porous SAPO-34 enhanced thin-film nanocomposite polymeric membrane: Simultaneously high water permeation and complete removal of cationic/anionic dyes from water, *J Hazard Mater.* 358 (2018) 376–388, https://doi.org/10.1016/j.jhazmat.2018.07.017.

[20] G. Zhao, R. Hu, Y. He, H. Zhu, Physically Coating Nanofiltration Membranes with Graphene Oxide Quantum Dots for Simultaneously Improved Water Permeability and Salt/Dye Rejection, *Adv Mater Interfaces.* 6 (5) (2019) 1801742, https://doi.org/10.1002/admi.201801742.

[21] G.S. Lai, W.J. Lau, P.S. Goh, A.F. Ismail, Y.H. Tan, C.Y. Chong, R. Krause-Rehberg, S. Awad, Tailor-made thin film nanocomposite membrane incorporated with graphene oxide using novel interfacial polymerization technique for enhanced water separation, *Chem Eng J.* 344 (2018) 524–534, https://doi.org/10.1016/j.cej.2018.03.116.

[22] R. Bi, Q. Zhang, R. Zhang, Y. Su, Z. Jiang, Thin film nanocomposite membranes incorporated with graphene quantum dots for high flux and antifouling property, *J Memb Sci.* 553 (2018) 17–24, https://doi.org/10.1016/j.memsci.2018.02.010.

[23] T. Zhang, P. Li, S. Ding, X. Wang, High permeability composite nanofiltration membrane assisted by introducing TpPa covalent organic frameworks interlayer with nanorods for desalination and NaCl/dye separation, *Sep Purif Technol.* 270 (2021) 118802, https://doi.org/10.1016/j.seppur.2021.118802.

[24] L. Yang, X. Zhang, W. Ma, B. Raisi, X. Liu, C. An, Z. Ye, Trimethylamine N-oxide-derived zwitterionic polyamide thin-film composite nanofiltration membranes with enhanced anti-dye deposition ability for efficient dye separation and recovery, *J Memb Sci.* 665 (2023) 121083, https://doi.org/10.1016/j.memsci.2022.121083.

[25] T. Ormanci-Acar, F. Celebi, B. Keskin, O. Mutlu-Salmanlı, M. Agtas, T. Turken, A. Tufani, D.Y. Imer, G.O. Ince, T.U. Demir, Y.Z. Menceloglu, S. Unal, I. Koyuncu, Fabrication and characterization of temperature and pH resistant thin film nanocomposite membranes embedded with halloysite nanotubes for dye rejection, *Desalination.* 429 (2018) 20–32, https://doi.org/10.1016/j.desal.2017.12.005.

[26] D. Ma, S.B. Peh, G. Han, S.B. Chen, Thin-Film Nanocomposite (TFN) Membranes Incorporated with Super-Hydrophilic Metal-Organic Framework (MOF) UiO-66: Toward Enhancement of Water Flux and Salt Rejection, *ACS Appl Mater Interfaces.* 9 (8) (2017) 7523–7534, https://doi.org/10.1021/acsami.6b14223.

[27] L. Ge, H. Song, J. Zhu, Y. Zhang, Z. Zhou, B. Van der Bruggen, Metal/covalent-organic framework based thin film nanocomposite membranes for advanced separations, *J Mater Chem A.* 12 (2024) 7975–8013, https://doi.org/10.1039/d4ta00578c.

[28] M. Peyravi, M. Jahanshahi, A. Rahimpour, A. Javadi, S. Hajavi, Novel thin film nanocomposite membranes incorporated with functionalized TiO_2 nanoparticles for organic solvent nanofiltration, *Chem Eng J.* 241 (2014) 155–166, https://doi.org/10.1016/j.cej.2013.12.024.

[29] L. Bai, Y. Liu, A. Ding, N. Ren, G. Li, H. Liang, Fabrication and characterization of thin-film composite (TFC) nanofiltration membranes incorporated with cellulose nanocrystals (CNCs) for enhanced desalination performance and dye removal, *Chem Eng J.* 358 (2019) 1519–1528, https://doi.org/10.1016/j.cej.2018.10.147.

[30] R.J. Moon, A. Martini, J. Nairn, J. Simonsen, J. Youngblood, Cellulose Nanomaterials Review: Structure, Properties and Nanocomposites, *Chem. Soc. Rev.* 40 (2011) 3941–3994, https://doi.org/10.1039/c0cs00108b.

[31] L. Bai, Y. Liu, N. Bossa, A. Ding, N. Ren, G. Li, H. Liang, M.R. Wiesner, Incorporation of Cellulose Nanocrystals (CNCs) into the Polyamide Layer of Thin-Film Composite (TFC) Nanofiltration Membranes for Enhanced Separation Performance and Antifouling Properties, *Environ Sci Technol.* 52 (19) (2018) 11178–11187, https://doi.org/10.1021/acs.est.8b04102.

[32] F. Asempour, D. Emadzadeh, T. Matsuura, B. Kruczek, Synthesis and characterization of novel Cellulose Nanocrystals-based Thin Film Nanocomposite membranes for reverse osmosis applications, *Desalination.* 439 (2018) 179–187, https://doi.org/10.1016/j.desal.2018.04.009.

[33] Y. Liu, L. Bai, X. Zhu, D. Xu, G. Li, H. Liang, M.R. Wiesner, The role of carboxylated cellulose nanocrystals placement in the performance of thin-film composite (TFC) membrane, *J Memb Sci.* 617 (2021) 118581, https://doi.org/10.1016/j.memsci.2020.118581.

[34] C. Xu, W. Chen, H. Gao, X. Xie, Y. Chen, Cellulose nanocrystal/silver (CNC/Ag) thin-film nanocomposite nanofiltration membranes with multifunctional properties, *Environ Sci Nano.* 7 (3) (2020) 803–816, https://doi.org/10.1039/c9en01367a.

[35] M. Peltzer, A. Pei, Q. Zhou, L. Berglund, A. Jiménez, Surface modification of cellulose nanocrystals by grafting with poly(lactic acid), *Polym Int.* 63 (6) (2014) 1056–1062, https://doi.org/10.1002/pi.4610.

[36] F. Abedi, M.A. Dubé, D. Emadzadeh, B. Kruczek, Improving nanofiltration performance using modified cellulose nanocrystal-based TFN membranes, *J Memb Sci.* 670 (2023) 121369, https://doi.org/10.1016/j.memsci.2023.121369.

[37] O. Azzaroni, Polymer brushes here, there, and everywhere: Recent advances in their practical applications and emerging opportunities in multiple research fields, *J Polym Sci Part A Polym Chem.* 50 (16) (2012) 3225–3258, https://doi.org/10.1002/pola.26119.

[38] B. Zhao, L. Zhu, Mixed Polymer Brush-Grafted Particles : A New Class of Environmentally Responsive Nanostructured Materials, *Macromol.* 42 (24) (2009) 9369–9383, https://doi.org/10.1021/ma902042x.

[39] J.J.K. Iv, J. Imbrogno, G. Belfort, Polymer Brushes for Membrane Separations: A Review, *ACS Appl. Mater. Interfaces* 8 (42) (2016) 28383–28399, https://doi.org/10.1021/acsami.6b09068.

[40] J.T. Mhlongo, M.L. Dlamini, Y. Nuapia, A. Etale, Synthesis and application of cationized cellulose for adsorption of anionic dyes, *Mater Today Proc*. 62 (2022) S133–S140, https://doi.org/10.1016/j.matpr.2022.02.100.
[41] F. Fahma, S. Iwamoto, N. Hori, T. Iwata, A. Takemura, Isolation, preparation, and characterization of nanofibers from oil palm empty-fruit-bunch (OPEFB), *Cellul.* 17 (5) (2010) 977–985, https://doi.org/10.1007/s10570-010-9436-4.
[42] Z. Zhang, X. Wang, K.C. Tam, G. Sèbe, A comparative study on grafting polymers from cellulose nanocrystals via surface-initiated atom transfer radical polymerization (ATRP) and activator re-generated by electron transfer ATRP, *Carbohydr Polym*. 205 (2019) 322–329, https://doi.org/10.1016/j.carbpol.2018.10.050.
[43] X. Zhang, J. Zhang, L. Dong, S. Ren, Q. Wu, T. Lei, Thermoresponsive poly(poly (ethylene glycol) methylacrylate)s grafted cellulose nanocrystals through SI-ATRP polymerization, *Cellul.* 24 (10) (2017) 4189–4203, https://doi.org/10.1007/s10570-017-1414-7.
[44] E.G. Masibi, T.A. Makhetha, R.M. Moutloali, Effect of the Incorporation of ZIF-8@GO into the Thin-Film Membrane on Salt Rejection and BSA Fouling, *Membranes (Basel)*. 12 (4) (2022) 436, https://doi.org/10.3390/membranes12040436.
[45] R. Hoffman, Solid-state chemical-shift referencing with adamantane, *J Magn Reson.* 340 (2022) 107231, https://doi.org/10.1016/j.jmr.2022.107231.
[46] A. Etale, D. Nhlane, J. Mhlongo, A. Khan, K. Rumbold, Y.B. Nuapia, Synthesis and Application of Cationised Cellulose for Removal of Cr (VI) from Acid Mine-Drainage Contaminated Water, *AAS Open Res*. 4 (2021) 4, https://doi.org/10.20944/preprints202009.0708.v1.
[47] Z. Abousalman-rezvani, P. Eskandari, H. Roghani-mamaqani, H. Mardani, M. Salami-Kalajahi, Grafting light-, temperature, and CO_2 -responsive copolymers from cellulose nanocrystals by atom transfer radical polymerization for adsorption of nitrate ions, *Polymer*. 182 (2019) 121830, https://doi.org/10.1016/j.polymer.2019.121830.
[48] W. Wu, F. Huang, S. Pan, W. Mu, X. Meng, H. Yang, Z. Xu, A.J. Ragauskas, Y. Deng, Thermo-Responsive and Fluorescent Cellulose Nanocrystals Grafted with Polymer Brushes, *J Mater Chem A*. 3 (2015) 1995–2005, https://doi.org/10.1039/b000000x.
[49] M.V. Kiriakou, R.M. Berry, T. Hoare, E.D. Cranston, Effect of Reaction Media on Grafting Hydrophobic Polymers from Cellulose Nanocrystals via Surface-Initiated Atom-Transfer Radical Polymerization, *Biomacromolecules*. 22 (8) (2021) 3601–3612, https://doi.org/10.1021/acs.biomac.1c00692.
[50] U.D. Hemraz, A. Lu, R. Sunasee, Y. Boluk, Structure of poly(N-isopropylacrylamide) brushes and steric stability of their grafted cellulose nanocrystal dispersions, *J Colloid Interface Sci*. 430 (2014) 157–165, https://doi.org/10.1016/j.jcis.2014.05.011.
[51] J. Yi, Q. Xu, X. Zhang, H. Zhang, Temperature-induced chiral nematic phase changes of suspensions of poly(N,N-dimethylaminoethyl methacrylate)-grafted cellulose nanocrystals, *Cellul.* 16 (6) (2009) 989–997, https://doi.org/10.1007/s10570-009-9350-9.
[52] E. Zeinali, V. Haddadi-Asl, H. Roghani-Mamaqani, Nanocrystalline cellulose grafted random copolymers of N- isopropylacrylamide and acrylic acid synthesized by RAFT polymerization: Effect of different acrylic acid contents on LCST behavior, *RSC Adv*. 4 (59) (2014) 31428–31442, https://doi.org/10.1039/c4ra05442c.
[53] S. Huang, L. Zhou, M.C. Li, Q. Wu, D. Zhou, Cellulose nanocrystals (CNCs) from corn stalk: Activation energy analysis, *Materials (Basel)* 10 (1) (2017), https://doi.org/10.3390/ma10010080.
[54] F. Hemmati, S.M. Jafari, M. Kashaninejad, M.M. Barani, Synthesis and characterization of cellulose nanocrystals derived from walnut shell agricultural residues, *Int J Biol Macromol*. 120 (2018) 1216–1224, https://doi.org/10.1016/j.ijbiomac.2018.09.012.
[55] M. Planes, J. Brand, S. Lewandowski, S. Remaury, S. Solé, C. Le Coz, S. Carlotti, G. Sèbe, Improvement of the Thermal and Optical Performances of Protective Polydimethylsiloxane Space Coatings with Cellulose Nanocrystal Additives, *ACS Appl Mater Interfaces*. 8 (41) (2016) 28030–28039, https://doi.org/10.1021/acsami.6b09043.
[56] X. Sui, J. Yuan, M. Zhou, J. Zhang, H. Yang, W. Yuan, Y. Wei, C. Pan, Synthesis of cellulose-graft-poly(N,N-dimethylamino-2-ethyl methacrylate) copolymers via homogeneous ATRP and their aggregates in aqueous media, *Biomacromolecules*. 9 (10) (2008) 2615–2620, https://doi.org/10.1021/bm800538d.
[57] Z. Zhang, G. Sèbe, X. Wang, K.C. Tam, UV-Absorbing Cellulose Nanocrystals as Functional Reinforcing Fillers in Poly(vinyl chloride) Films, *ACS Appl Nano Mater*. 1 (2) (2018) 632–641, https://doi.org/10.1021/acsanm.7b00126.
[58] M.C.D. Ngaha, L.G. Djemmoe, E. Njanja, I.T. Kenfack, Biosorption Isotherms and Kinetics Studies for the Removal of 2,6-Dichlorophenolindophenol Using Palm Tree Trunk ((Elaeis guineensis), *J Encapsulation Adsorpt Sci*. 8 (3) (2018) 156–177, https://doi.org/10.4236/jeas.2018.83008.
[59] L.L. Borba, R.M.F. Cuba, F.J. Cuba Terán, M.N. Castro, T.A. Mendes, Use of adsorbent biochar from pequi (Caryocar Brasiliense) husks for the removal of commercial formulation of glyphosate from aqueous media, *Brazilian Arch Biol Technol.* 62 (2019), https://doi.org/10.1590/1678-4324-2019180450.
[60] Y. Wang, D. Wilson, G.S. Harbison, Solid-State NMR and the Crystallization of Aspartic and Glutamic Acids, *Cryst Growth Des*. 16 (2) (2016) 625–631, https://doi.org/10.1021/acs.cgd.5b01052.
[61] Q. Xie, S. Zhang, Z. Xiao, X. Hu, Z. Hong, R. Yi, W. Shao, Q. Wang, Preparation and characterization of novel alkali-resistant nanofiltration membranes with enhanced permeation and antifouling properties: the effects of functionalized graphene nanosheets, *RSC Adv*. 7 (30) (2017) 18755–18764, https://doi.org/10.1039/c7ra00928c.
[62] U. Sharma, R. Pandey, S. Basu, P. Saravanan, Facile monomer interlayered MOF based thin film nanocomposite for efficient arsenic separation, *Chemosphere*. 309 (P1) (2022) 136634, https://doi.org/10.1016/j.chemosphere.2022.136634.
[63] M. Bagherzadeh, M. Nikkhoo, M.M. Ahadian, M. Amini, Novel Thin-Film Nanocomposite Forward Osmosis Membranes Modified with WS_2/CuAl LDH Nanocomposite to Enhance Desalination and Anti-fouling Performance, *J Inorg Organomet Polym Mater*. 33 (4) (2023) 956–968, https://doi.org/10.1007/s10904-023-02547-6.
[64] G. Natesan, K. Rajappan, GO–CuO nanocomposites assimilated into CA–PES polymer membrane in adsorptive removal of organic dyes from wastewater, *Environ Sci Pollut Res*. 30 (15) (2023) 42658–42678, https://doi.org/10.1007/s11356-022-21821-7.
[65] M. Wasim, A. Sabir, M. Shafiq, A. Islam, M. Azam, T. Jamil, Mixed matrix membranes: Two step process modified with electrospun (carboxy methylcellulose sodium salt/sepiolite) fibers for nanofiltration, *J Ind Eng Chem*. 50 (2017) 172–182, https://doi.org/10.1016/j.jiec.2017.02.011.
[66] D. Chen, Q. Chen, T. Liu, J. Kang, R. Xu, Y. Cao, M. Xiang, Influence of L-arginine on performances of polyamide thin- film composite reverse osmosis membranes, *RSC Adv*. 9 (2019) 20149–20160, https://doi.org/10.1039/c9ra02922b.
[67] K.C. Wong, P.S. Goh, A.F. Ismail, Highly permeable and selective graphene oxide-enabled thin film nanocomposite for carbon dioxide separation, *Int J Greenh Gas Control.* 64 (2017) 257–266, https://doi.org/10.1016/j.ijggc.2017.08.005.
[68] W. Zhao, H. Liu, N. Meng, M. Jian, H. Wang, X. Zhang, Graphene oxide incorporated thin film nanocomposite membrane at low concentration monomers, *J Memb Sci*. 565 (2018) 380–389, https://doi.org/10.1016/j.memsci.2018.08.047.
[69] S. Liu, Z.X. Low, H.M. Hegab, Z. Xie, R. Ou, G. Yang, G.P. Simon, X. Zhang, L. Zhang, H. Wang, Enhancement of desalination performance of thin-film nanocomposite membrane by cellulose nanofibers, *J Memb Sci*. 592 (2019) 117363, https://doi.org/10.1016/j.memsci.2019.117363.
[70] M.T. Hoang, T.D. Pham, D. Verheyen, M.K. Nguyen, T.T. Pham, J. Zhu, B. Van der Bruggen, Fabrication of thin film nanocomposite nanofiltration membrane incorporated with cellulose nanocrystals for removal of Cu (II) and Pb (II), *Chem Eng Sci*. 228 (2020) 115998, https://doi.org/10.1016/j.ces.2020.115998.
[71] M. Kadhom, N. Albayati, S. Salih, M. Al-Furaiji, M. Bayati, B. Deng, Role of cellulose micro and nano crystals in thin film and support layer of nanocomposite membranes for brackish water desalination, *Membranes (Basel)* 9 (8) (2019), https://doi.org/10.3390/membranes9080101.
[72] R. Goswami, M. Gogoi, A. Borah, H. Sarmah, A.R. Borah, X. Feng, S. Hazarika, Quantum dot- β-Cyclodextrin nanofiller decorated thin film nanocomposite membrane for removal of cationic and anionic dyes from aqueous solution, *Mater Today Chem*. 35 (2024) 101871, https://doi.org/10.1016/j.mtchem.2023.101871.
[73] B. Sapkota, W. Liang, A. VahidMohammadi, R. Karnik, A. Noy, M. Wanunu, High permeability sub-nanometre sieve composite MoS_2 membranes, *Nat Commun*. 11 (1) (2020) 2747, https://doi.org/10.1038/s41467-020-16577-y.
[74] A. Akbari, P. Sheath, S.T. Martin, D.B. Shinde, M. Shaibani, P.C. Banerjee, R. Tkacz, D. Bhattacharyya, M. Majumder, Large-area graphene-based nanofiltration membranes by shear alignment of discotic nematic liquid crystals of graphene oxide, *Nat Commun*. 7 (2016) 10891, https://doi.org/10.1038/ncomms10891.
[75] H. Abadikhah, E.N. Kalali, S. Khodi, X. Xu, S. Agathopoulos, Multifunctional Thin-Film Nanofiltration Membrane Incorporated with Reduced Graphene Oxide@TiO_2@Ag Nanocomposites for High Desalination Performance, Dye Retention, and Antibacterial Properties, *ACS Appl Mater Interfaces*. 11 (26) (2019) 23535–23545, https://doi.org/10.1021/acsami.9b03557.
[76] L. Yang, X. Liu, X. Zhang, T. Chen, Z. Ye, M.S. Rahaman, High performance nanocomposite nanofiltration membranes with polydopamine-modified cellulose nanocrystals for efficient dye/salt separation, *Desalination*. 521 (2022) 115385, https://doi.org/10.1016/j.desal.2021.115385.
[77] E.R. Nightingale, Phenomenological theory of ion solvation. Effective radii of hydrated ions, *J. Phys. Chem*. 63 (1959) 1381–1387.
[78] B. Liu, S. Zhang, Z. Yao, L. Dong, Y. Bai, C. Zhang, Carbon Nitride Quantum Dot-Based Thin-Film Nanocomposite Membranes for Efficient Dye Removal, *ACS Appl Nano Mater*. 6 (18) (2023) 16297–16308, https://doi.org/10.1021/acsanm.3c02401.
[79] M. Borpatra Gohain, S. Karki, D. Yadav, A. Yadav, N.R. Thakare, S. Hazarika, H. K. Lee, P.G. Ingole, Development of Antifouling Thin-Film Composite/Nanocomposite Membranes for Removal of Phosphate and Malachite Green Dye, *Membranes (Basel)*. 12 (8) (2022) 768, https://doi.org/10.3390/membranes12080768.
[80] M.-M. Jia, J.-H. Feng, W. Shao, Z. Chen, J.-R. Yu, J.-J. Sun, Q.-Y. Wu, Y. Li, M. Xue, X.-M. Chen, In-situ interfacial synthesis of metal-organic framework/polyamide thin-film nanocomposite membranes with elevated nanofiltration performances, *J Memb Sci.* 694 (2024) 122418, https://doi.org/10.1016/j.memsci.2024.122418.
[81] C. Zhou, H. Li, L. Wang, T. Fu, G. Liu, X. Shen, H. Zhao, High-flux and stability nanofiltration membranes prepared with β-cyclodextrin and in-situ co-polymerized of TpPa COFs for dye desalination, *J. Environ. Chem. Eng*. 13 (2025) 116096, https://doi.org/10.1016/j.jece:2025.116096.
[82] Z. Qin, S. Xiang, Z. Jing, M. Deng, W. Jiang, L. Yao, L. Yang, L. Deng, Z. Dai, Thin film nanocomposite membranes fabricated via 2D ZIF-67 nanosheets and 1D nanofibers with ultrahigh water flux for dye removal from wastewater, *Sep Purif Technol.* 330 (2025) 125308, https://doi.org/10.1016/j.seppur.2023.125308.